A new sea ice albedo scheme including melt ponds for ECHAM5 general circulation model

Christina A. Pedersen,[1,2] Erich Roeckner,[3] Mikael Lüthje,[4] and Jan-Gunnar Winther[1]

Received 16 May 2008; revised 18 November 2008; accepted 5 February 2009; published 16 April 2009.

[1] Today we experience an accelerated melting of sea ice in the Arctic which global circulation models are inadequate to predict. We believe one of the reasons is the shortcomings in the sea ice albedo schemes for these models. This paper investigates a physically based sea ice albedo scheme for ECHAM5 GCM, which separates between snow-covered sea ice, bare sea ice, melt ponds, and open water (separately for the albedos and albedo fractions). The new albedo scheme includes important components such as albedo decay due to snow aging, bare sea ice albedo dependent on the ice thickness, and a melt pond albedo dependent on the melt pond depth. The explicit treatment of melt pond albedos has, to our knowledge, not been included in general circulation models before and represents a substantial improvement when simulating the annual cycle of sea ice albedo. The new albedo scheme overall reduces the sea ice albedo both in winter, because of snow aging, and in summer, because of melt ponds. The reduced sea ice albedo leads to overall reduced sea ice thickness, concentration, and volume, with large temporal and spatial variations. In the Northern Hemisphere in March, some areas experience increased albedo, resulting in thicker sea ice and higher ice concentration, but in August the pattern is spatially homogeneous, with reduced albedo, thickness, and concentrations for all areas where the new scheme has a significant effect.

Citation: Pedersen, C. A., E. Roeckner, M. Lüthje, and J.-G. Winther (2009), A new sea ice albedo scheme including melt ponds for ECHAM5 general circulation model, *J. Geophys. Res.*, *114*, D08101, doi:10.1029/2008JD010440.

1. Introduction

[2] The average temperature in the Arctic has increased at twice the rate of the global average the last 100 years (IPPC AR4 [*Solomon et al.*, 2007]), and with the increased warming, we have seen substantial decreases in both sea ice extent [*Comiso*, 2006] and thickness [*Gerland et al.*, 2007]. The September Arctic sea ice extent declined with an average rate of 7.8% per decade over the last 50 years [*Stroeve et al.*, 2007], with an accelerated rate of 8.6% per decade over the last 17 years [*Comiso*, 2006]. In contrast to the Arctic, the Antarctic sea ice cover has been gradually and slightly increasing during the last 28 years [*Cavalieri and Parkinson*, 2008].

[3] Snow and sea ice covered surfaces have a high albedo, and are important for the climate whenever large areas are exposed to significant solar energy. Sea ice is particularly sensitive to moderate temperature changes as a warmer climate will expose surrounding surfaces of substantially lower albedo, e.g., open water at the expenses of sea ice. This results in most of the incoming sunlight being absorbed, which again leads to further warming. This amplifies the warming and creates a positive feedback [*Curry et al.*, 1995; *Morassutti*, 1991].

[4] The sea ice albedo feedback is important for the energy balance in general circulation models (GCMs). All GCMs used in the Intergovernmental Panel on Climate Change Fourth Assessment Report (IPCC AR4) show declining Arctic sea ice over the last 50 years. However, none (or very few) of the models show trends comparable to the recent observations (depending on the investigated scale) [*Stroeve et al.*, 2007]. Traditionally, GCMs have treated high-latitude cryospheric processes quite crudely. A wide variety of snow and sea ice albedo parameterizations schemes are currently used in GCMs, see, e.g., *Pedersen and Winther* [2005], *Curry et al.* [2001], or *Barry* [1996] for an overview. Most schemes are very simplistic, depending only on surface type and temperature. A few schemes include snow depth and ice thickness, and even fewer include spectral and solar angle dependencies. However, most GCMs use the sea ice albedo as a tuning parameter [*Curry et al.*, 2001]. Previous studies have shown that today's GCMs are unable to capture the annual cycle of sea ice albedo, particularly in summer where the GCMs overestimate the albedo [*Køltzow*, 2007; *Wang et al.*, 2006; *Curry et al.*, 2001].

[5] A correct representation of sea ice albedo in GCMs is necessary to incorporate the physical processes involved in the formation and melting of snow and sea ice. It has previously been shown that more advanced schemes allows

[1]Norwegian Polar Institute, Tromsø, Norway.
[2]Also at Department of Mathematics and Statistics, University of Tromsø, Tromsø, Norway.
[3]Max Planck Institute for Meteorology, Hamburg, Germany.
[4]SINTEF Petroleum Research, Stavanger, Norway.

0148-0227/09/2008JD010440

for larger albedo feedbacks [*Curry et al.*, 2001]. During the northern hemisphere summer, solar radiation melts the snow and the upper surface of the sea ice. This produces melt water which later transforms into melt ponds on the ice. These melt ponds substantially reduce the surface albedo and absorb two to three times more solar energy compared to thick bare sea ice [*Fetterer and Untersteiner*, 1998b].

[6] Melt ponds have been investigated at several locations in the Arctic over the years, from the surface [*Tucker et al.*, 1999; *Fetterer and Untersteiner*, 1998b; *Perovich and Tucker*, 1997], from air [*Perovich et al.*, 2002b; *Tschudi et al.*, 2001; *Derksen et al.*, 1997] and from space [*Markus et al.*, 2002, 2003; *Hanesiak et al.*, 2001b; *Yackel and Barber*, 2000]. Also, the seasonal evolution of melt ponds has been modeled [*Lüthje et al.*, 2006; *Taylor and Feltham*, 2004]. The above mentioned studies indicate a melt pond fraction ranging from 5–80% depending on surface roughness, snow cover, ice type, time of year, and location. The spatial distribution of melt ponds depends on the topography of the snow and sea ice. First year ice (FYI) tends to be smoother than multiyear ice (MYI), and melt ponds on FYI are normally less deep [*Morassutti and LeDrew*, 1996], but cover a larger area [*Hanesiak et al.*, 2001a]. The formation of melt ponds on FYI is strongly correlated with the winter distribution of snow, and areas of little snow accumulation during winter are preferred places for melt ponds to form [*Hanesiak et al.*, 2001a; *Derksen et al.*, 1997]. On the rougher MYI the melt ponds form in depressions, and tend to be smaller, deeper and more numerous.

[7] In this paper we take advantage of knowledge from the model community [*Lüthje et al.*, 2006; *Taylor and Feltham*, 2004] and combine it with information extracted from field data [*Pedersen et al.*, 2009; *Brandt et al.*, 2005; *Gerland et al.*, 2004; *Perovich et al.*, 2002b; *Gerland et al.*, 1999; *Morassutti and LeDrew*, 1996] to propose a new, more physically based sea ice albedo parameterization scheme for the ECHAM5 GCM [*Roeckner et al.*, 2003, 2006]. The scheme separates between four surface types (snow-covered ice, bare ice, melt ponds and open water) and determines the albedo and fraction of these types separately. To the best of our knowledge, it is the first time a physical description of melt pond albedo is included explicitly in any GCM. In short, section 2.1 describes the original temperature-dependent sea ice albedo scheme for ECHAM5, while the new scheme's components are presented in section 2.2. Results and intercomparisons of simulations with both the old and the new schemes, assessing both time series and spatial distributions, are given in section 3. Emphasis is placed on the inclusion of melt ponds. A discussion of the results and conclusions are given in section 4.

2. Model Description

[8] The coupled model consists of new model versions for both the atmosphere and the ocean. In the atmospheric model (ECHAM5 [*Roeckner et al.*, 2003, 2006]) vorticity, divergence, temperature, and the logarithm of surface pressure are represented by truncated series of spherical harmonics, whereas the advection of water vapor, cloud liquid water, and cloud ice are treated by a flux-form semi-Lagrangian scheme. A hybrid sigma/pressure system is used in the vertical direction. The model uses detailed parameterizations for shortwave and longwave radiation, stratiform clouds, cumulus convection, boundary layer, land surface processes, and gravity wave drag.

[9] The ocean model (MPI-OM) [*Marsland et al.*, 2003] employs the primitive equations for a hydrostatic Boussinesq fluid with a free surface. The parameterization of physical processes include along-isopycnal diffusion, horizontal tracer mixing by advection with unresolved eddies, vertical eddy mixing, near-surface wind stirring, convective overturning, and slope convection. The dynamics of sea ice are formulated using viscous-plastic rheology following *Hibler* [1979]. The thermodynamics relate changes in sea ice thickness to a balance of radiant, turbulent, and oceanic heat fluxes. The effect of snow accumulation on sea ice is included, along with snow-ice formation when the snow/ice interface sinks below the sea level because of snow loading. The effect of ice formation and melting is accounted for within the model.

[10] In the coupled model [*Jungclaus et al.*, 2006], the ocean passes to the atmosphere the sea surface temperature, sea ice concentration, sea ice thickness, snow depth on ice, and the ocean surface velocities. The atmosphere runs with these boundary values for one coupling time step (1 day) and accumulates the forcing fluxes. These fluxes are then transferred to the ocean. All fluxes are calculated separately for ice-covered and open water portions of the grid cells. River runoff and glacier calving are treated interactively in the atmosphere model and the respective fresh water fluxes are passed to the ocean together with the atmospheric precipitation minus evaporation field. The model does not employ flux adjustments.

2.1. Original Sea Ice Albedo Scheme

[11] The original sea ice albedo scheme is a function of the ice surface temperature T_i. The albedo is determined from a linear interpolation between a low albedo ($\alpha_{i,\min}$) at the melting point ($T_i = T_0$) and a high albedo ($\alpha_{i,\max}$) at low temperatures, ($T_i = T_d$), where $T_d = T_0 - 1$, and

$$\alpha_i = \alpha_{i,\min} + \left(\alpha_{i,\max} - \alpha_{i,\min}\right) f(T_i) \tag{1}$$

$$f(T_i) = \min\left(\max\left(\frac{T_0 - T_i}{T_0 - T_d}, 0\right), 1\right). \tag{2}$$

The extreme albedos, $\alpha_{i,\min}$ and $\alpha_{i,\max}$, are defined separately for bare ice and snow-covered ice (Table 1).

2.2. New Sea Ice Albedo Scheme

[12] We follow the structure of the complex albedo parameterization in a small-scale thermodynamic sea ice model [*Schramm et al.*, 1997] to construct a new sea ice albedo scheme for the four surface types; snow-covered sea ice (α_s), bare sea ice (α_i), melt ponds (α_{mp}) and open water (α_w). The total albedo is weighted according to the grid mean ice concentration

$$\alpha = \alpha_{ice} f_{ice} + \alpha_w (1 - f_{ice}), \tag{3}$$

where f_{ice} is the sea ice concentration from ECHAM5. The sea ice albedo is defined as

$$\alpha_{\text{ice}} = \alpha_s f_s + \alpha_i f_i + \alpha_{mp} f_{mp}. \tag{4}$$

Table 1. Parameters for the Original Sea Ice Albedo Scheme for ECHAM5

Surface Type	$\alpha_{i,\min}$	$\alpha_{i,\max}$
Snow-covered sea ice	0.60	0.80
Bare sea ice	0.50	0.75

The snow cover fraction (f_s) is calculated from the snow depth (ECHAM5's original description [*Roesch et al.*, 2001]), the melt pond fraction (f_{mp}) from the melt pond depth (discussed in section 2.2.3), and the bare ice fraction (f_i) is extracted from the sum of the others.

[13] In the latest version of ECHAM5, the number of spectral bands has been increased to six (three bands in the UV-visible (VIS) and three bands in the near-infrared (NIR)). We use one parameterization for the three VIS bands and another for the three NIR bands. The broadband albedo is calculated by weighting the VIS and NIR albedos with the irradiance spectra. Separate schemes are developed for the diffuse and direct components of the solar radiation, and weighted according to the cloud cover fraction computed in ECHAM5. The individual albedo components, described in the next sections, are also summarized in Table 2. The wavelength ranges for the different schemes differ slightly from the wavelength range used in ECHAM5; however, the solar spectrum is roughly divided at 700 nm for all schemes.

2.2.1. Snow-Covered Sea Ice

[14] Two main groups of snow albedo schemes are common in GCMs: temperature-dependent schemes (including ECHAM5) and prognostic schemes. In a previous study the temperature-dependent schemes were found not to capture the winter snow metamorphosis and spring melting very well as the albedo was fixed to threshold values [*Pedersen and Winther*, 2005]. The prognostic schemes have an iterative albedo dependence, with separate decay factors for melting and nonmelting snow, and reset the albedo to its maximum after new snowfall above a prescribed precipitation threshold. They are found to capture the seasonal cycle better than the temperature-dependent schemes [*Pedersen and Winther*, 2005].

[15] Both types of schemes were originally created for snow on land, but can be used for snow-covered sea ice, by compensating for an underlying surface of bare ice. We suggest to replace the original, empirical temperature-dependent scheme in ECHAM5 with the more physically based prognostic scheme BATS (Biosphere-Atmosphere Transfer Scheme [*Dickinson et al.*, 1986]). BATS includes all processes relevant to capturing the changes in snow albedo, and it separates between VIS and NIR bands, as well as between diffuse and direct radiation. It was shown to accurately represent the temporal snow albedo decay when implemented in ECHAM4. In fact, BATS was the preferred snow albedo scheme for ECHAM4 [*Roesch*, 2000]. The BATS snow scheme has been validated against observations by *Roesch* [2000] and *Yang et al.* [1997], with good correspondence.

2.2.2. Bare Sea Ice

[16] We take advantage of the extensive sets of sea ice albedos collected by *Brandt et al.* [2005] in the Antarctic sea ice zone over several years. The spectral albedos for different sea ice types were measured and integrated to obtain VIS ($\lambda <$ 700 nm) and NIR ($\lambda >$ 700 nm) sea ice albedos. As clouds only weakly absorb at VIS wavelengths, the visible albedo is the same under cloudy and clear skies, while for NIR, the observations were split into a diffuse and direct component. On the basis of *Brandt et al.* [2005], we propose a simple least squares fit parameterization of the form

$$\alpha_i = a \cdot \log(h_i) + b, \tag{5}$$

where a and b are the model parameters and h_i is the ice thickness in cm (Figure 1 and Table 3). For ice thicknesses equal to or above 1.6 m for VIS and 1.0 m for NIR, the upper threshold values from Table 3 are used.

2.2.3. Melt Ponds

[17] The inclusion of melt ponds in the albedo scheme is very important from a physical perspective, because of their extensive presence during summer [*Perovich et al.*, 2002b; *Tschudi et al.*, 2001; *Fetterer and Untersteiner*, 1998b; *Perovich and Tucker*, 1997], and the large portion of solar energy absorbed by the melt water [*Podgorny and Grenfell*, 1996]. Both *Schramm et al.* [1997] and *Morassutti and LeDrew* [1996] provide useful melt pond albedo parameterizations as a function of pond depth. However, such schemes cannot be used directly because melt pond depth, and also the more important melt pond fraction (see equation (4)), is not available in GCMs.

[18] We propose a basic model for melt pond evolution based on the daily surface ice melt rate from ECHAM5. The temporal evolution of a melt pond is calculated from the mass balance equation

$$\frac{\partial p_d}{\partial t} = -\frac{\rho_i}{\rho_w}\left(\frac{\partial h_i}{\partial t} + \frac{\partial p_{di}}{\partial t}\right) - \left(\frac{\partial p_d}{\partial t}\right)_s, \tag{6}$$

Table 2. New Sea Ice Albedo Parameterization Scheme in ECHAM5[a]

Albedo of Surface Type	VIS 250–690 nm	NIR 690–4000 nm
Snow-covered sea ice, α_s		
Direct	BATS equations	BATS equations
Diffuse	BATS equations	BATS equations
Bare sea ice, α_i	0.13 $\ln(h_i)$ + 0.10[b]	
Direct		0.047 $\ln(h_i)$ + 0.074[b]
Diffuse		0.049 $\ln(h_i)$ + 0.085[b]
Melt pond, α_{mp}		
Direct	0.336 + exp(−9.457 d_{mp}−1.061)	0.017 + exp(−18.904 d_{mp}−0.909)
Diffuse	0.413 + exp(−24.014 d_{mp}−1.086)	0.061+ exp(−17.449 d_{mp}−1.075)

[a]Scheme separates between snow-covered sea ice (α_s), bare sea ice (α_i), melt ponds (α_{mp}), and open water (corresponding to ECHAM5's original, and therefore not repeated here) for visible (VIS) and near-infrared (NIR) bands and diffuse and direct radiation. h_i is the ice thickness in cm, and d_{mp} is the melt pond depth in m. BATS equations from *Dickinson et al.* [1986].
[b]For ice thicknesses equal to or above 1.6 m for VIS and 1.0 m for NIR, constant albedos of 0.76 for VIS and 0.29 for NIR direct and 0.31 for NIR diffuse are used.

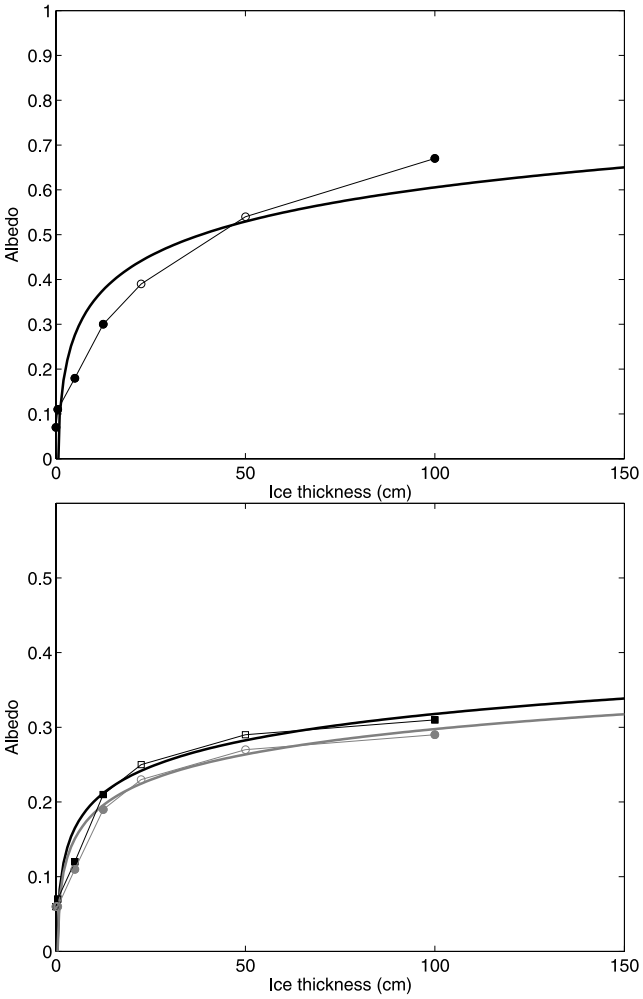

Figure 1. Sea ice albedo as a function of ice thickness for (top) visible (VIS, $\lambda < 700$ nm) and (bottom) near-infrared (NIR, $\lambda > 700$ nm) spectral bands after *Brandt et al.* [2005]. The filled symbols are measurements, while the open are interpolated values. The depths are the mean of the range of each sea ice type. The thick solid line is the least mean squares fit of the form $\alpha_i = a \log(h_i) + b$, where a and b are given in Table 3. A distinction is made between direct (black) and diffuse (gray) irradiance for NIR in Figure 1 (bottom).

where p_d is the pond depth in m and ρ_w, ρ_i are the densities of water and ice, respectively (Figure 2). The first term on the right hand side represents the melt pond growth through the surface melting of sea ice; the second term refers to the growth or melting of pond ice (p_{di}); and the last term is the constant seepage rate. Pond ice forms if the temperature of the pond, T_w, falls below the freezing point, T_0, where T_w is calculated from the heat budget equation

$$C_w \frac{\partial T_w}{\partial t} = H_{sfc}. \tag{7}$$

C_w is the heat capacity of the pond and H_{sfc} is the sum of all radiative and turbulent heat fluxes at the surface of the ice-free pond. For $T_w < T_0$, a slab of ice is formed according to

$$p_{di} = \left(\frac{C_w}{L_f \rho_i}\right)(T_0 - T_w), \tag{8}$$

Table 3. Constants for Bare Sea Ice Albedo[a]

	a	b	Upper Threshold
VIS	0.13	0.10	0.76
NIR direct	0.047	0.074	0.29
NIR diffuse	0.049	0.085	0.31

[a]Bare sea ice albedo is of the form $\alpha_i = a \log(h_i) + b$ proposed from data from *Brandt et al.* [2005] for visible (VIS, $\lambda < 700$ nm) and near-infrared (NIR, $\lambda > 700$ nm) (direct and diffuse). The upper threshold values are used for ice thicknesses equal to or above 1.6 m for VIS and 1.0 m for NIR.

where L_f is the latent heat of fusion. T_w is then reset to T_0 and is kept fixed, independent of the sign of H_{sfc}, because the pond water is forming on top of the ice. The surface temperature of the ice, T_i, is calculated from the heat budget of a thin slab of ice (1 cm) at the surface

$$C_i \frac{\partial T_i}{\partial t} = H_{sfc} + H_c, \tag{9}$$

where C_i is the heat capacity of the thin upper slab of pond ice and H_c is the conductive heat flux through the ice given by

$$H_c = \frac{\kappa_i}{p_{di}}(T_0 - T_i) \geq 0, \tag{10}$$

where κ_i is the thermal conductivity of ice.

[19] Melt pond formation will not start before the snow on top of the sea ice has melted away. If a slab of pond ice $p_{di} \geq 1$ cm is forming, the melt pond fraction is set to zero. The final closing of the melt pond in fall is generally caused by vanishing melting and constant seepage, resulting in $p_d \leq 0$, or by freezing if the pond is totally frozen or if a thick ice layer has been formed ($p_{di} = 10$ cm). In all these cases the pond is closed, i.e., p_d is set to zero.

[20] To provide an estimate of the melt pond fraction, we propose to calculate it from the melt pond depth (similar to what is done for the snow cover fraction in GCMs) using a parameterization of the results from a number of simulations using a small-scale melt pond model [*Lüthje et al.*, 2006]. This model is, to our knowledge, the only published model that calculates the depth and fraction covered by melt ponds during the melt season. The model treats the ice surface as a porous medium. Melt water drains through the ice to the ocean at a constant rate (0.8 cm/d) and the melt water left on the surface percolates to lower lying areas to form melt ponds. The melt rate is kept constant during the melt season,

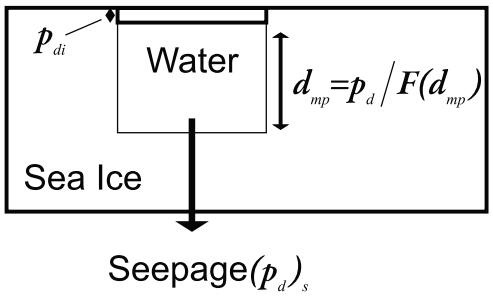

Figure 2. A schematic drawing of a melt pond describing a few of the variables in equations (6)–(10).

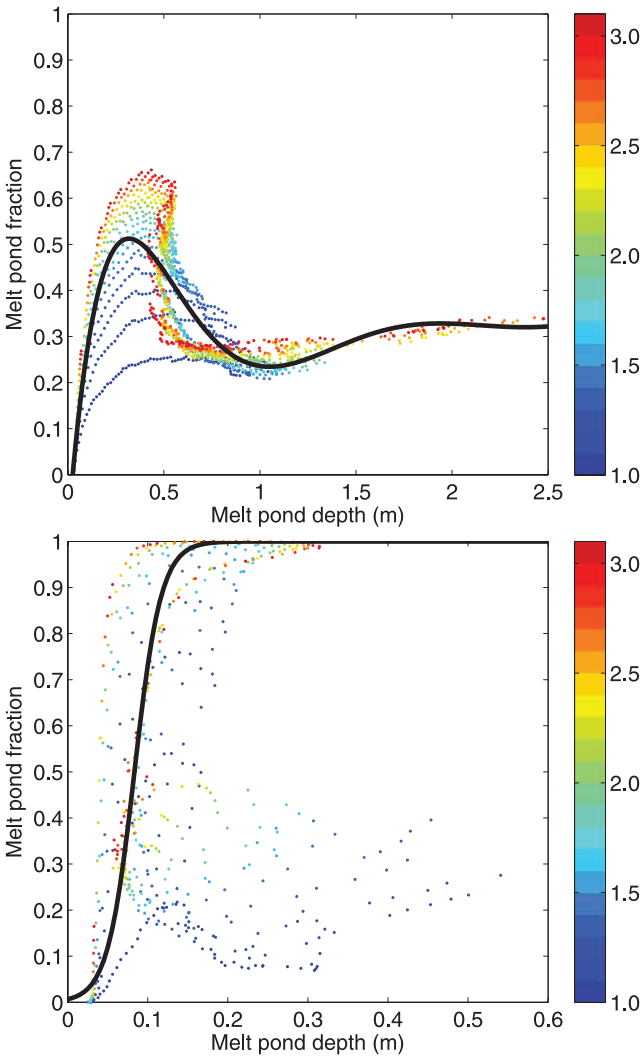

Figure 3. Melt pond depth versus melt pond fraction for (top) multiyear ice (MYI) and (bottom) first year ice (FYI). The thick lines represents the best fit to the data. For MYI the best fit is represented by a 8-degree polynomial (equation (11)), and for FYI it is represented by a hyperbolic tangent (equation (12)). The scatter plot is based on the melt pond model by *Lüthje et al.* [2006] by using melt rates ranging from 1 cm/d to 3 cm/d (in steps of 0.1 cm/d) as indicated by the color bar.

but is enhanced where melt ponds forms, to simulate the lower albedo of the melt ponds. The model discretizes the space and time domain using a finite differences scheme. For relating the melt pond depth and fraction covered for different climate scenarios, the model was run with the same input parameters as described in details by *Lüthje et al.* [2006]. The melt rate for the ice surface was varied from 1.0 cm/d to 3.0 cm/d (in steps of 0.1 cm/d), while the enhanced melt rate under the melt ponds was kept at twice the ice surface melt rate. This was done for both a MYI and a FYI setting, resulting in a total of 42 model runs, with a melt season of 71 days. The mean daily fraction of the surface covered by melt ponds is plotted against the daily mean melt pond depth in Figure 3 (for FYI and MYI separately).

[21] To connect the melt pond fraction to the melt pond depth for MYI (Figure 3, top), an 8-degree polynomial was fitted to the data points:

$$f_{mp} = a \cdot d_{mp}^8 + b \cdot d_{mp}^7 + c \cdot d_{mp}^6 + d \cdot d_{mp}^5 + e \cdot d_{mp}^4 + f \cdot d_{mp}^3 + g \cdot d_{mp}^2 + h \cdot d_{mp} + i \quad (11)$$

where d_{mp} is the melt pond depth in m, and the constants (a–i) are given in Table 4. Figure 3 (top) shows melt pond depths up to 2.5 m for unrealistically high melt rates (2.5–3.0 cm/d) during the end of the 71 simulated days. Such depths are not realistic, and were only included to avoid reaching outside the range of possible melt pond depth. For FYI, the connection between fraction and depth is more complex (Figure 3, bottom). For small melt rates, the relationship is similar to that for MYI, but for more realistic melt rates, the relationship is better described by a hyperbolic tangent function,

$$f_{mp} = 0.5 \tanh\left(30 d_{mp} - 2.5\right) + 0.5. \quad (12)$$

Since melt ponds on FYI are mostly important in the beginning and middle of the melt season, before the ice breaks up, the fit is created to correspond best with this data, and less with the model data from later in the melt season.

[22] Regression equations were used for calculating the melt pond albedo from melt pond depth from observations of melt pond albedo in the Canadian Arctic Archipelago in spring and summer by *Morassutti and LeDrew* [1996]:

$$\alpha_{mp} = a + \exp\left(-b \cdot d_{mp} - c\right), \quad (13)$$

where a, b, and c are regression coefficients, determined for VIS (400–700 nm) and NIR (700–1000 nm) bands under different light conditions (Table 5). The exponential albedo decay is large for the first 10–20 cm of pond depth, and for deeper melt ponds the albedo is relatively constant.

3. Results

[23] Two model experiments were performed using a low-resolution version of ECHAM5/MPI-OM [*Jungclaus et al.*, 2006]. The atmospheric component, ECHAM5, has a horizontal resolution of T31, corresponding to a grid of 3.75° × 3.75°, with 19 layers in the vertical. The oceanic component, MPI-OM, has a horizontal resolution of 3° and 40 layers in the vertical. In the first experiment (CTL), the original temperature-dependent sea ice albedo scheme was used. In the second experiment (ALB), the new albedo

Table 4. Constants for Melt Pond Fraction as a Function of Melt Pond Depth for Multiyear Ice[a]

a	b	c	d	e	f	g	h	i
−0.00724636	0.14438	−1.19140	5.25995	−13.37101	19.53030	−15.27019	5.26674	−0.12549

[a]See equation (11).

Table 5. Constants for Melt Pond Albedo[a]

	a	b	c
VIS direct	0.336	9.457	1.061
VIS diffuse	0.413	24.014	1.086
NIR direct	0.017	18.904	0.909
NIR diffuse	0.061	17.449	1.075

[a]Melt pond albedo (α_{mp}) is of the form $\alpha_{mp} = a + \exp(-b \cdot d_{mp} - c)$ as a function of melt pond depth (d_{mp}) from *Morassutti and LeDrew* [1996] for visible (VIS) and near-infrared (NIR) and direct and diffuse radiation.

scheme was applied. In both experiments the atmospheric composition of greenhouse gases and aerosols were prescribed at constant preindustrial conditions. This approach results in robust statistics as the model is in steady state. The experiments started from the same initial state, obtained from a multicentury simulation with the standard configuration of the model, and were both run for 100 years. During this period the drift in global mean climate parameters was negligible. For the analysis, only the last 50 years of the simulations were considered. The climatological means as well as the standard deviations shown in Figures 5, 6, and 8–12 refer to this 50-year time series.

3.1. Seasonal Cycles

3.1.1. One Year Seasonal Cycle

[24] The seasonal cycle of the new albedo scheme was first investigated for a single sea ice covered grid cell for 1 year. The chosen grid cell was within the multiyear sea ice, at 76°N and 165°W (i.e., the SHEBA site during summer 1998 [*Perovich et al.*, 1999], described later). The snow cover fraction was one until mid-June, hence the sea ice albedo is completely determined by the prognostic snow albedo scheme, and fluctuates because of the aging of the snow and new snow fall (Figure 4, top). The basic aging factor f_{age} in the BATS snow albedo scheme [*Dickinson et al.*, 1986] is never completely reset to zero during winter (however, it reaches values down to 0.02 after large snow events). From May onward the aging parameter increases, and in mid-June it reaches its maximum above 0.7, resulting in a steady decay in albedo. The snow cover fraction drops from one to zero in a short time period in mid-June, when the snow depth drops from 4 to 0 cm snow water equivalent (SWE), coinciding with the steep decay in snow albedo at the same time. Simultaneously, the bare ice fraction jumps to one, giving an albedo completely determined by the ice albedo. In mid-July, melt water creates melt ponds on the ice. As the fraction of melt ponds increases and the melt ponds get deeper, the surface albedo decreases. The melt pond fraction peaks in early August. In the end of August the ponds drain, and the melt pond fraction decreases. Light snowfall in the beginning of September increases the albedo. The first autumn snowfall provides only 1 cm SWE, however such a thin snow cover is often inhomogeneous, and the snow cover fraction is only about 0.15. For ECHAM5, a snow depth above 3 cm SWE gives a snow cover fraction of one, implying "optically thick" snow [*Wiscombe and Warren*, 1980]. In mid September, a major snow event increases the snow cover fraction to one and provides albedos comparable to premelting conditions.

[25] Some clear differences are identified by comparing the new ALB with the old CTL albedo schemes (Figure 4, top). CTL is constant at 0.8 when temperatures are below freezing, hence it is basically at this value from mid-September until June, with only one drop in mid-May due to a short period of high temperatures, while the ALB albedo varies because of snow aging and new snow falls (mean albedo of 0.79 from January–May). In spring when the surface temperature rises above zero, and the snow cover fraction is still at one, the CTL albedo is immediately fixed to its lower snow value. For snow free conditions, the CTL albedo is completely determined by the sea ice albedo, fluctuating between 0.5 and 0.75 depending on the surface temperature. Hence the CTL albedo is higher than the ALB albedo during most of the summer. Particularly, in spring and fall, the ALB albedo deviates substantially from CTL albedo; in late summer ALB albedo is much lower because of the inclusions of melt ponds.

[26] The chosen grid cell within the multiyear ice (average ice thickness of 3 m), includes the positions of the SHEBA ice camp in summer in 1998 [*Perovich et al.*, 1999]. The seasonal evolution of the albedo from the SHEBA site is thoroughly discussed by *Perovich et al.* [2002a], and consists of five distinct phases: dry snow, melting snow, melt pond

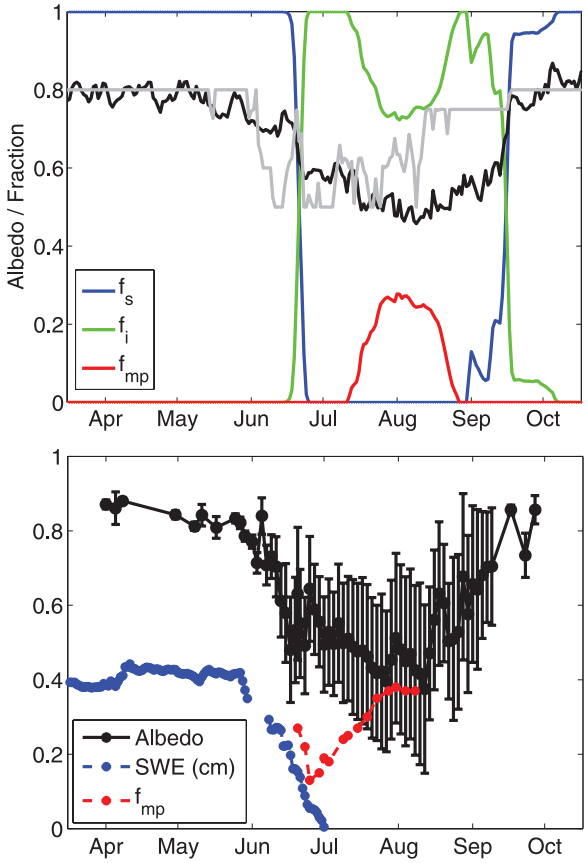

Figure 4. (top) Seasonal cycle of sea ice albedo for the new (ALB, black) and old (CTL, gray) schemes at the SHEBA site in the multiyear ice Arctic Ocean. Also shown are the area fractions (snow cover fraction, f_s; bare sea ice fraction, f_i; melt pond fraction, f_{mp}). (bottom) Seasonal cycle of observed sea ice albedo (mean and standard deviations in black) along the 200 m "albedo line" at SHEBA in 1998. Also shown are the snow depth (in SWE) for winter/spring and the melt pond fractions.

Table 6. Fraction of Ice in the NH Covered by Melt Ponds in the New Albedo Scheme[a]

	All	MYI	FYI	SHEBA
Monthly mean	25.7%	19.7%	77.0%	19.0%
Monthly max	36.2%	31.6%	95.0%	48.0%
Daily max	48.3%	43.5%	99.7%	51.2%
Mean daily max	37.8%	31.2%	93.3%	28.6%
Monthly min	14.5%	11.0%	47.9%	0.0%
Daily min	3.0%	1.1%	7.7%	0.0%
Mean daily min	8.2%	5.7%	28.4%	5.1%

[a]The fraction is given for all ice (all), for multiyear ice (MYI), for first year ice (FYI), and for the SHEBA site (SHEBA). The fractions are given as a monthly mean value for July (monthly mean), the monthly maximum value (monthly max), the maximum daily occurrence in all 50 years (daily max), and the mean of the maximum daily occurrences for the 50 years (mean daily max). Similarly for the minimum values.

formation, melt pond evolution and fall freezeup (Figure 4, bottom). The SHEBA albedo was a combination of gradual changes due to seasonal evolutions and abrupt changes due to synoptic weather events. A different mixture of sea ice types along the albedo line would only change the magnitude of the albedo, not the temporal behavior [*Perovich et al.*, 2002a], so it is appropriate to compare the ALB time series with this. However, keep in mind that the modeled albedo cycle cannot be linked to any particular year.

[27] The ALB albedo corresponds well with the SHEBA observations (SHEBA—The Surface Heat Budget of the Arctic Ocean: Snow and Ice Studies, CD-ROM, version 1.1, October 1999) in terms of trends, with a correlation coefficient of 0.83, and an average root-mean-square error of 0.08. The absolute numbers are not of immense importance as a delay of spring melting and/or fall freezeup can appear in either of the two data sets because of interannual variability and synoptic weather events. The ALB albedo is lower than the observed albedos at SHEBA when snow is present, while in summer, it is higher. Both time series show a rather steep decline in the albedo starting in late spring and reaching its minimum when the melt pond fraction reaches its maximum. However, the abrupt change is a combination of melting snow and formation of melt ponds in SHEBA [*Perovich et al.*, 2002a], while it is linked to melting of the snow and decreasing snow cover fraction in ECHAM5. Since the melting of snow coincided with the melt pond formation in SHEBA it is difficult to separate the two effects. Recall that melt ponds do not form in the model before the snow is completely melted. The average melt pond coverage over the entire melt season at SHEBA was 32% for level MYI and 13% for rough MYI [*Eicken et al.*, 2004]. These measurements are in approximate accordance with the modeled average coverage of melt ponds of 19% for MYI in July. The maximum coverage differs for the 50 modeled years and ranges between a single year where no ponds formed to a maximum of 51% (Table 6). The overall mean maximum modeled coverage was 28.6%, agreeing well with the observed maximum coverage for rough MYI (21%) and level MYI (46%) [*Eicken et al.*, 2004]. The modeled mean melt pond depth of 35 cm in August also fits well with observations (Surface Heat Energy Balance of the Arctic Ocean: Melt ponds, available at http://www.crrel.usace.army.mil/sid/perovich/SHEBAice/meltpond.htm, accessed December 2007).

3.1.2. Average Seasonal Cycles

[28] The average area fractions of snow-covered sea ice, bare ice, and melt ponds for the 50 years over the Northern Hemisphere (NH, Figure 5, top) differ from the 1 year cycle in the grid cell discussed above. The abrupt changes in the 1 year time series are replaced with more gradual changes. The NH winter is mostly characterized by snow-covered sea ice, but because of temporal and spatial averaging, the snow fraction is below one during winter, as weather events may bring warm air which melts away the snow near the ice edges. In July and August the bare ice fraction is at its maximum at 0.72 ± 0.03, while the snow fraction is at its minimum. The standard deviations of the snow-covered and bare ice fractions are small and relatively constant at 0.05 during the entire year. Some melt ponds start to form in May and some are present until September. The mean coverage for July is 25.7% with a daily maximum and minimum of 48.3% and 3%. On average, 19.7% of the MYI (max: 43.5%; min: 1.1%) and 77.0% of the FYI (max: 99.7%; min: 7.7%) is covered by melt ponds in July (Table 6). These results agree well with observations showing that melt ponds in the NH typically cover around 20–35% of MYI [*Tschudi et al.*, 2001; *Fetterer and Untersteiner*, 1998a;

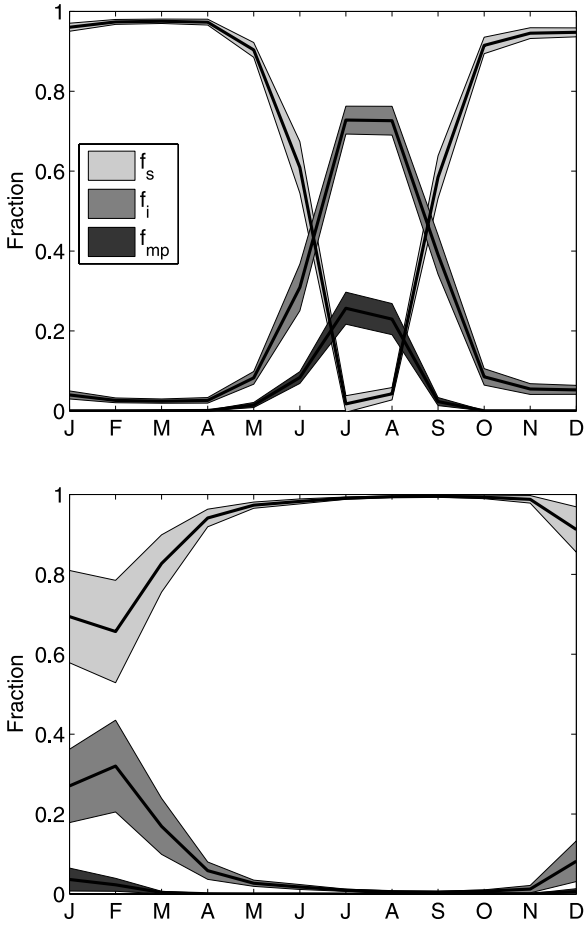

Figure 5. Fifty-year average seasonal cycles of area fractions of snow-covered ice, f_s; bare ice, f_i; and melt ponds, f_{mp}, and standard deviations (as shades) for (top) the Northern Hemisphere and (bottom) the Southern Hemisphere for the new ALB albedo scheme.

Tschudi et al., 1997] and 45–80% of FYI [*Yackel and Barber*, 2000; *Yackel et al.*, 2000; *Barber and Yackel*, 1999]. Observations show peak melt pond coverage up to almost 100% on FYI, again in correspondence with the modeled maximum coverage (Table 6). The average melt pond depth was 54.4 cm. The ponds on MYI were deeper (62.0 cm) than the ponds on FYI (37.4 cm), also in correspondence with observations showing that melt ponds on FYI are shallower than on MYI [*Morassutti and LeDrew*, 1996]. *Yackel et al.* [2000] reported FYI and MYI maximum melt pond depths of around 40 cm and 65 cm, respectively.

[29] The area fractions show a completely different pattern in the Southern Hemisphere (SH, Figure 5, bottom), with large variability in the snow-covered and bare ice fractions in Antarctic summer (January and February). This may be due to the large interannual variability, with much snow in relatively cold summers and less snow in warm summers on the ice edges. Melt ponds cover a much smaller area in the SH, and are only present in January and February, with a mean coverage of 4% for these months. Observations of melt pond coverage in the SH are very limited, but the overall coverage is small [*Brandt et al.*, 2005; *Andreas and Ackley*, 1982; C. Haas, personal communication, 2007] because the ice tends to melt predominantly from the bottom because of a higher heat flux from the ocean. In the long Antarctic winter snow completely covers the sea ice, with snow cover fraction as high as 0.995 in September (different from the relatively lower snow cover fraction in NH in winter).

[30] The annual mean sea ice albedo is 0.66 in the NH and 0.76 in the SH, with standard deviations of 0.04 and 0.01 (Figure 6, top) for the new scheme (ALB). Overall, the ALB scheme reduces the NH sea ice albedo in all seasons, with as much as 10% on average in summer (May to October). The largest reductions (23% and 15%) appear in August and September. During the polar night, the sea ice albedo shown in Figure 6 is not representative for the whole NH and SH. In November and December, for example, sea ice formation to the south of the polar circle is limited to a few areas like Hudson Bay and along the East Siberian coast. This explains the rather low values and large interannual variability of the NH sea ice albedo during these months. In spring, the ALB scheme has a lower albedo than CTL as a result of snow aging (the parameterization of the snow cover fraction is identical in CTL and ALB). During these months the snow albedo has the potential to drop to low values, especially during warm and dry spells with hardly any snowfall. On the other hand, fresh snowfall will reset the snow albedo to its maximum value. These processes are of immense importance, and we plan to investigate these further in sensitivity experiments. In fall and early winter the open water areas are refrozen and compaction increases. Although the total NH sea ice areas show little interannual variability in November and December (Figure 6, middle), there might be regional variability due to atmospheric and/or ocean dynamics.

[31] For SH, the seasonal sea ice albedo cycle is relatively weak, with albedos above 0.7 for all months, except January and February; consequently, the albedo reduction from the new scheme is less pronounced. The winter snow albedo is higher in SH compared to NH, because the snow aging in BATS is smaller in SH compared to NH (the parameter describing the effect of dirt and soot, r_3, is 0.01 in SH, and

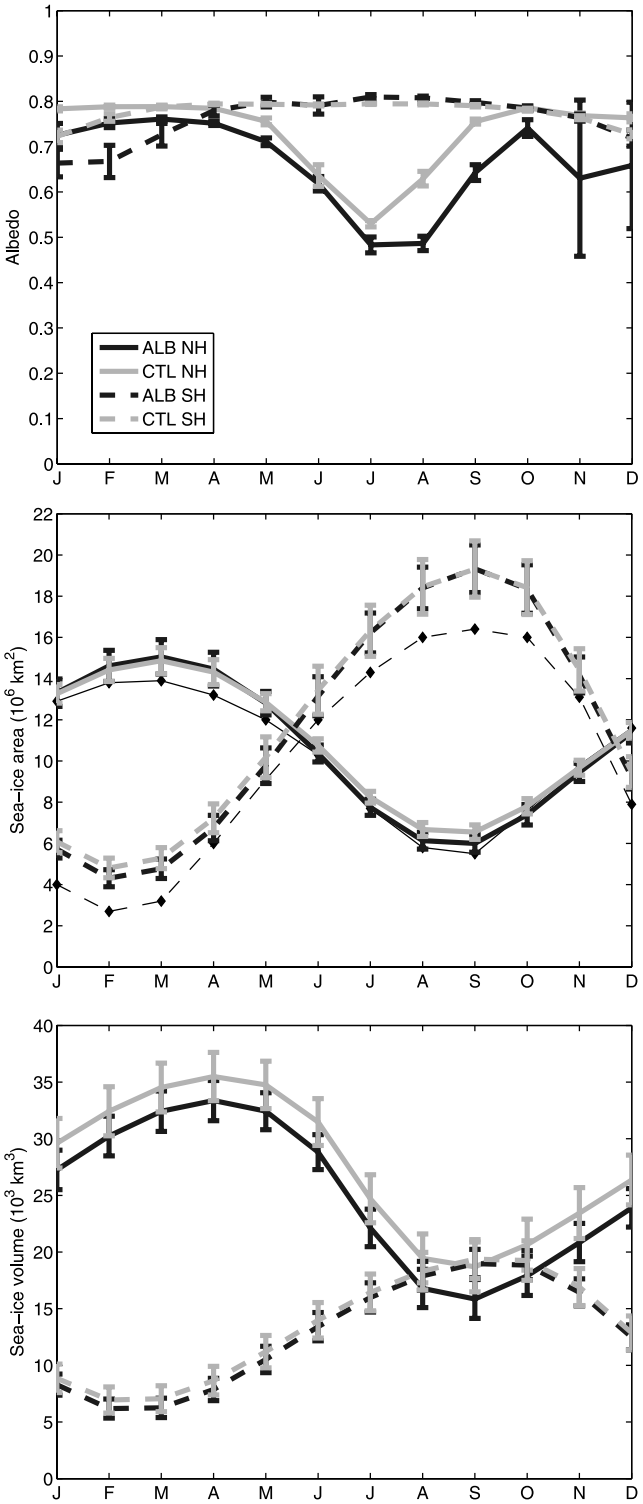

Figure 6. 50 years means and standard deviations (as error bars) of (top) sea ice albedo, (middle) sea ice area, and (bottom) sea ice volume for the old (CTL) and new (ALB) albedo scheme for Northern Hemisphere (NH) and Southern Hemisphere (SH). The diamonds in Figure 6 (middle) are average sea ice area from HadISST [*Rayner et al.*, 2003].

Figure 7. Area mask of the Arctic basin marginal seas and seasonal ice zones from *Overland and Wang* [2007].

0.3 in NH [*Dickinson et al.*, 1993]). In SH summer the maximum albedo reduction due to the new scheme is 13%. As the melt pond fraction is relatively small compared to NH in summer, the decrease in albedo is probably a combination of the formation of melt ponds on the ice and the reduced snow albedo due to snow aging and relatively high temperatures. For May and July–November, the ALB albedo scheme slightly increases the albedo compared to the CTL scheme (on average a 1% rise).

[32] The seasonal cycles of sea ice area in the ALB scheme, which are very similar to those with the CTL scheme, have maxima of 15.1×10^6 km^2 in March for NH and 19.3×10^6 km^2 in September for SH, and minimums of 6.0×10^6 km^2 in September for NH and 4.3×10^6 km^2 in February for SH (Figure 6, middle). The seasonal cycle in the SH spans a larger range, implying that the SH has substantially more FYI compared to the NH. The new ALB scheme leads to increased sea ice area in NH winter (on average 1%). From May onward the effect is opposite with reduced sea ice area. The largest reductions are found in August and September with 8% reductions. The effect of the new scheme ALB in SH is reduced sea ice area for all months, except September, which has a small increase. The differences are largest in February and March with an average sea ice area reduction of 10%.

[33] Compared to HADISST sea ice area [*Rayner et al.*, 2003] over the years 1979–2002 the seasonal cycle is in phase (correlation coefficients are over 0.99 for both NH and SH), but with slightly different amplitudes. Overall the sea ice areas from model simulations (both ALB and CTL) are higher than the HADISST area (particularly for SH), except for June–July and October–December in NH, where the ALB scheme matches HADISST or are slightly lower, respectively. Overall, the ALB scheme is 3.7% higher than HadISST for NH and as much as 16.1% higher for SH. The difference between present and preindustrial climate may, however, be responsible for some of this deviation.

[34] The annual mean sea ice volume is 25.2×10^3 km^3 for the NH and 12.8×10^3 km^3 for the SH, with standard deviations of 1.70×10^3 km^3 and 1.12×10^3 km^3, respectively (Figure 6, bottom). The new ALB scheme affects the sea ice volume substantially more in NH than SH. The annual average volume decreases 10% for NH compared to 5% for SH. The reductions in volume are relatively larger than reductions in sea ice areas, particularly for NH, because of large reductions in ice thickness (discussed later).

3.2. Spatial Distributions

[35] We just showed that the new ALB scheme overall reduced the sea ice albedo, area, and volume, mostly in the

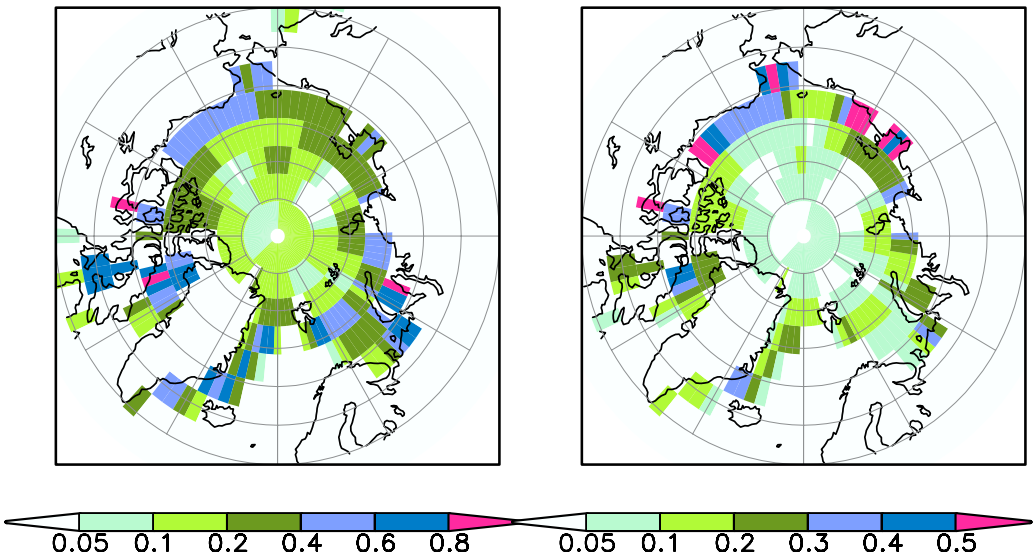

Figure 8. Spatial variabilities of (left) the melt pond fractions and (right) the melt pond depths averaged over the sea ice area (p_d, m) for the Northern Hemisphere for July.

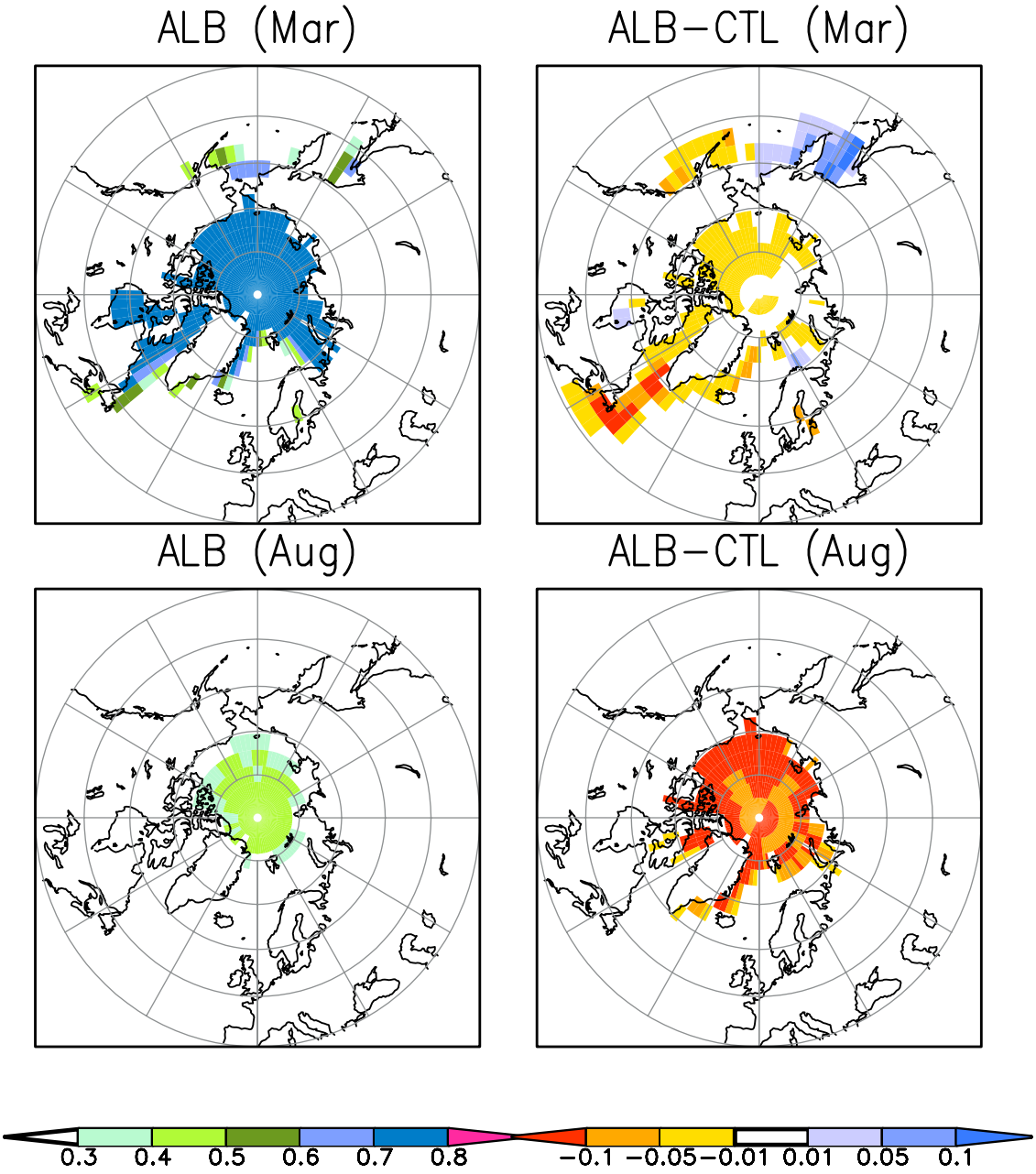

Figure 9. (left) Sea ice albedo (excluding open water) in the Northern Hemisphere for the new albedo scheme (ALB) and (right) the difference between the new and old albedo scheme (ALB-CTL) for (top) March and (bottom) August.

NH, and mostly in summer. Next we will investigate the spatial distributions, concentrating on the NH. When describing the areas in NH we will use the area mask of the Arctic Basin marginal seas and seasonal ice zones from *Overland and Wang* [2007] (Figure 7).

[36] To investigate if the changes introduced by the new albedo scheme are in fact of statistical significance, an adapted statistical scale-space technique [*Pedersen et al.*, 2008] has been applied on the difference field between the sea ice parameters from the ALB and CTL schemes. The scale-space technique provides maps of areas of statistical significance at different spatial scales for a given confidence level (here the common 5% is used). The scaling issue is introduced since at finer scales there is usually a large amount of noise, whereas successively coarser scales smooth the data and reduce noise. However, at very coarse scales interesting features can be smoothed away entirely. The scales investigated here are 280 km, 1100 km, 2500 km, and 4000 km.

3.2.1. Melt Ponds

[37] Figure 8 (left) shows for the first time a modeled estimate of the spatial variability of the melt pond coverage. As expected, the spatial pattern shows that most melt ponds are found close to land because of a higher fraction of FYI. The highest fractions are found in southern Barents, north-

Table 7. Fifty-Year Average Northern Hemisphere Sea Ice Albedo in Models and Observations[a]

	June	July	August	June–August
CTL	57.8	44.7	50.3	51.0
ALB	56.1	41.6	38.9	45.5
OBS	52.7	40.3	43.7	45.6

[a]Including leads. CTL, the old scheme; ALB, the new scheme; OBS, observations from *Laine* [2004].

ern Baffin Labrador, and along east Greenland. North of 80°N the fractional coverage is smaller since mostly MYI is present. The deepest melt ponds are found in the E. Siberia Chukchi and Beaufort, whereas the melt ponds are shallower to the north (Figure 8, right).

3.2.2. Sea Ice Albedo

[38] The sea ice albedo is high (average 0.78) and relatively homogeneous over the Central Arctic in March (Figure 9). The ALB scheme reduces the albedo everywhere compared to CTL, except in Okhotsk and small areas north of Norway and in Hudson Bay, where the ALB scheme leads to increased albedos. For some areas in Central Arctic and Kara Laptev no changes are evident. The albedo reductions are significant only in Beaufort (for all investigated scales). For August, the ice covered areas are substantially smaller, with reduced albedo everywhere (average reductions of 0.1). The reductions are significant for the entire Arctic Basin for the two coarsest scales (2500 km and 4000 km), and in southern Beaufort and E. Siberia Chukchi also for finer scales com-

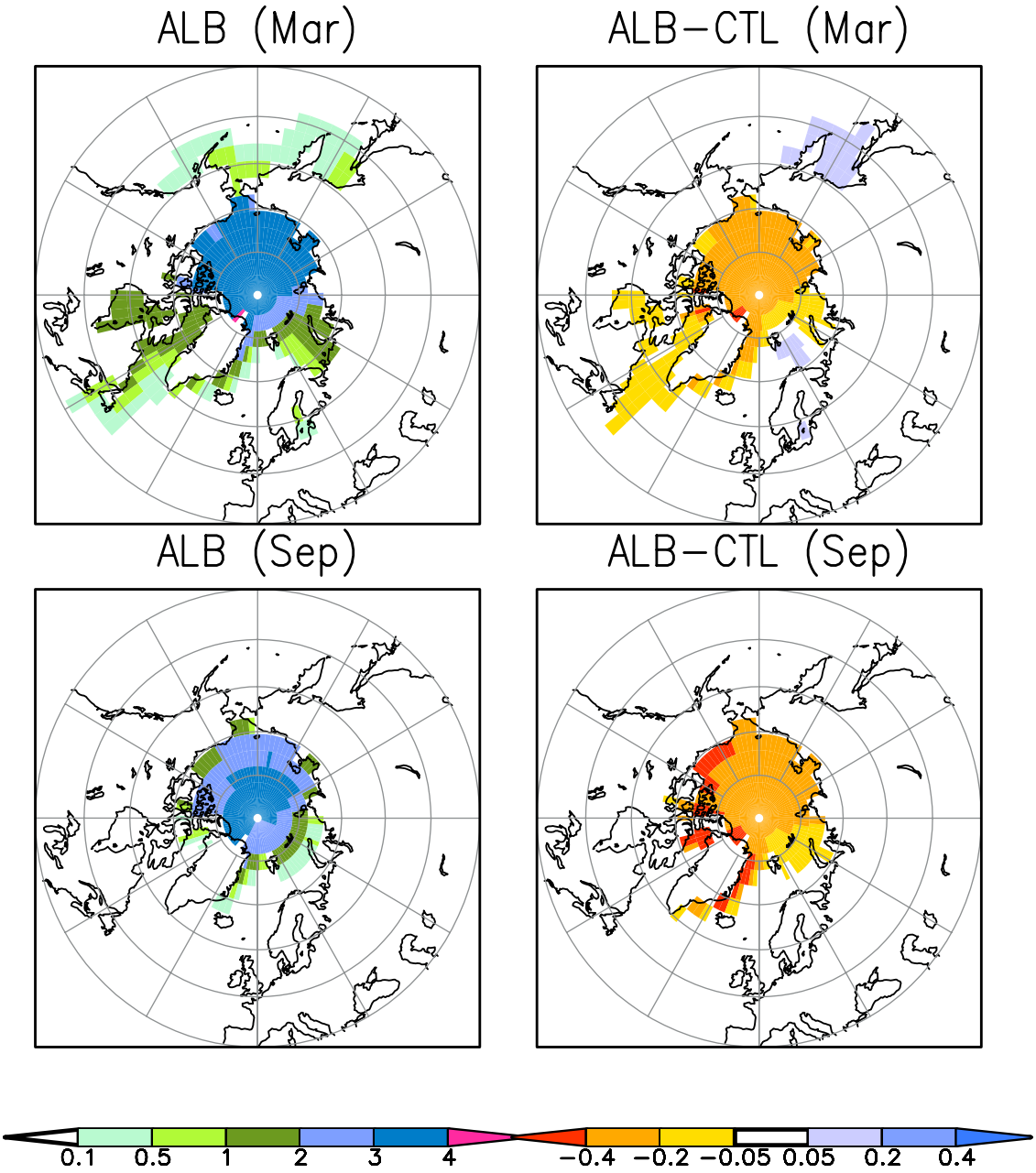

Figure 10. (left) Sea ice thickness (m) in the Northern Hemisphere for the new albedo scheme (ALB) and (right) the difference between the new and old albedo scheme (ALB-CTL) for (top) March and (bottom) September.

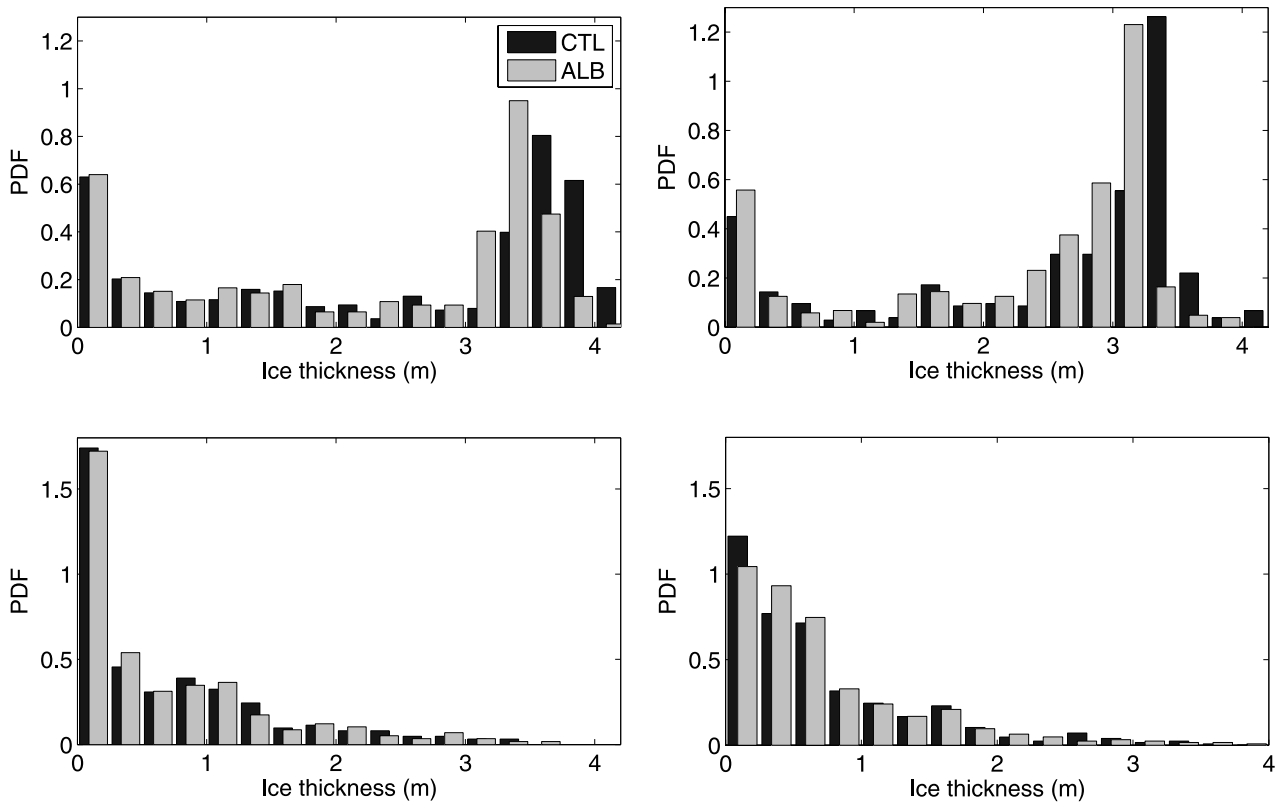

Figure 11. Probability density functions (PDFs) for sea ice thickness in the old (CTL) and new (ALB) albedo schemes for Northern Hemisphere in (top left) March and (top right) September and for Southern Hemisphere in (bottom left) March and (bottom right) September.

parable to the grid cell size (280 km). The average sea ice albedo in the Central Arctic in August is 0.45, and around 0.3 on the ice edge. For some areas, e.g., around the south and east coast of Greenland, ALB completely melts the ice, hence the albedo reductions are substantial.

[39] Both schemes generally overestimate the albedo compared to observations [*Laine*, 2004] (Table 7). However, the new scheme reduces the albedo during summer (June–August), thus reducing the bias. On average, the new scheme matches the observations very well.

[40] Some areas of difference are found for SH summer (January–March) in the Weddell Sea, where ALB albedo is significantly lower than CTL albedo for the two coarsest scales (not shown). In winter (August) a few pixels are found in the Weddell Sea and Ross Sea where the ALB albedo are significantly higher than the CTL albedo for the coarsest scale, i.e., opposite of the general trend.

3.2.3. Sea Ice Thickness

[41] The average sea ice thickness in the Central Arctic from the ALB scheme is around 3.3 m in March, and is reduced by 0.2–0.3 m in September (Figure 10). The ice is thickest in the E. Siberia Chukchi and in Central Arctic toward Greenland and east Canada in March, corresponding well with other data sets with thicknesses up to 4.0 m [*McLaren et al.*, 2006]. Thin ice in March is found south of 70°N in the Bering Sea and western part of North Atlantic Ocean. In September, the thin FYI has melted, and thin ice is found only in small areas in the Barents Sea, northern Baffin Labrador, and along the eastern coast of Greenland. Overall, the ALB scheme reduces the ice thickness, except for the Barents and Okhotsk, where the ice thickness is slightly increased in March. The absolute reductions are largest for the thick ice in the Central Arctic and smallest on the ice edge in March. In September, the ice thickness is reduced everywhere, with largest reductions for the thin ice areas in Beaufort and East Greenland. The absolute changes are smallest at the thin ice areas in Barents. The pattern of significant ice thickness reductions is similar for March and September, where the albedo in Central Arctic, Baffin Labrador, Beaufort and E. Siberia Chukchi are significant for the two coarser scales.

[42] It is, however, difficult to validate the distribution and seasonal cycles of sea ice thickness, because of the lack of consistent ice thickness data sets. A previous study using satellite altimeter measurements of ice freeboard [*Laxon et al.*, 2003], found the average winter ice thickness (excluding thin ice below 1 m) over sea ice areas for NH south of 81.5°N for the period 1993–2001 to be 2.7 m. The thickest ice was observed in the Canadian Archipelago and in the Fram Strait.

[43] The probability density functions (PDFs) show in a clear way the difference between the ice thickness distributions for ALB and CTL (Figure 11). The PDFs for NH have a bimodal distribution, with the first peak at 0.13 m for ALB and CTL, and the second peak at 3.38 m and 3.63 m for ALB and CTL in March. In September the second peak is slightly shifted toward thinner ice. For NH, the ALB scheme leads to more thin ice and less thick ice. The ice thickness

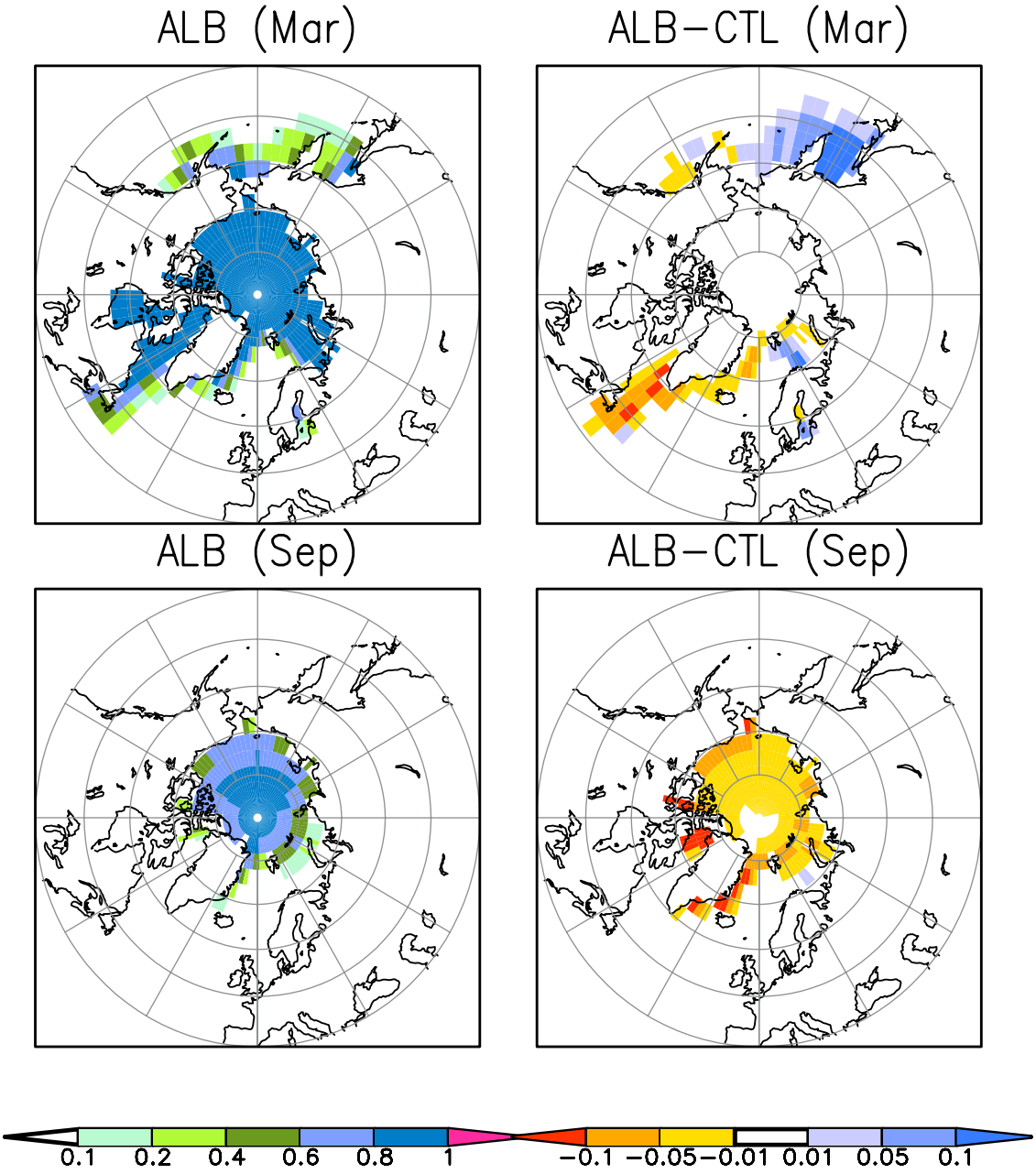

Figure 12. (left) Sea ice concentration (%) in the Northern Hemisphere for the new albedo scheme (ALB) and (right) the difference between the new and old albedo scheme (ALB-CTL) for (top) March and (bottom) September.

distribution for the SH is unimodal, with a peak for thin ice and very little thick ice (because of most of the sea ice in the SH being FYI). The frequency of the thin ice is slightly reduced with the ALB scheme (opposite of what we see in NH), and a slight increase in intermediate ice thicknesses can be seen, but changes in SH PDFs are small.

3.2.4. Sea Ice Concentration

[44] The NH sea ice area has a strong seasonal cycle (Figure 6, middle), with sea ice covering almost the whole Arctic Basin in March (Figure 12). In September, all the FYI has melted and the ice is mainly concentrated north of 70°N, and even farther north for areas affected by the North Atlantic Current. In March, the ALB scheme reduces the sea ice concentration south and east of Greenland, but increases it in Barents, Bearing, and Okhotsk. However, none of these changes are significant. The overall effect is increased concentrations in winter. In May there is a shift, and the overall effect becomes reduced concentrations (Figure 6, middle). In September, the concentration is reduced along the coastal areas (by as much as 0.2 in northern Baffin Labrador and the east coast of Greenland), but not in the central Arctic itself. Only for small areas in Baffin Labrador the concentration reductions are significant for the two coarsest scales. The areas with large changes have strong interannual variability, and relatively low ice concentrations.

[45] In the SH, neither the ice thickness nor ice area reductions are statistically significant. This confirms the previous results that melt ponds are dominant in the NH, and play a minor role in the SH.

4. Discussion and Conclusions

[46] It has previously been recognized that GCMs are unable to predict the annual cycle of sea ice albedo completely; in particular the albedo is too large in summer [*Køltzow*, 2007; *Curry et al.*, 2001]. *Wang et al.* [2006] found that the IPCC AR4 climate models systematically overestimate the sea ice albedo in summer by as much as 0.05.

[47] We have developed a new physically based sea ice albedo parameterization scheme for the ECHAM5 GCM following the structure of the sea ice albedo in a small-scale thermodynamic sea ice model [*Schramm et al.*, 1997], which separates between snow-covered sea ice, bare sea ice, melt ponds, and open water. To the authors knowledge, no GCM has included an explicit, physical treatment of melt ponds on sea ice before. Despite the relatively short duration of melt ponds, they contribute significantly to the energy balance because the albedo effect on the climate is largest in summer.

[48] Compared to the old (CTL) albedo scheme, the new scheme (ALB) was found to reduce the sea ice albedo both in winter, because of snow aging, and in summer, because of melt ponds. In addition, the spring decay and autumn increase of sea ice albedo were captured in a more realistic way in the new scheme. The new albedo parameterization scheme simulated the annual cycle of sea ice albedo in a realistic way, capturing the important changes that determine the onset of melt, the duration of melt, and the start of the fall freezeup. The correlation coefficient between the 1 year sea ice albedo simulations (ALB) and 1 year observations at the SHEBA site [*Perovich et al.*, 2002a] was 0.83, where the ALB albedo was slightly higher than the observed albedo in summer. The SHEBA albedo may, however, represent a lower boundary for albedo during summer, since when compared to the albedo from several decades of Soviet NP drifting ice stations data, SHEBA albedo was slightly lower than the monthly minimum albedo for mid-June to mid-September [*Perovich et al.*, 2002a].

[49] The new albedo scheme performed well in modeling the coverage of melt ponds compared to the observations at the SHEBA site, both when looking at the temporal evolution and the mean area covered. For the entire NH, the coverage was on the low side compared to observations, but gave for the first time an estimate of the spatial variability of the melt pond coverage. The reductions in albedo were predominantly in the FYI areas, as melt ponds tend to cover larger areas on FYI. The melt ponds tend to be shallower on FYI, but the many shallow melt ponds on FYI reduce the albedo more than the fewer deeper ponds on MYI because melt ponds covered a total of 77% of the area on FYI in July, but only 20% on the MYI. There was large interannual variability in the ECHAM5 model. This implies there were years when hardly any melt ponds formed, while in others the formation of melt ponds started already in early June and reached depths up to 0.5 m in August. The melt pond fraction was at its maximum in July, with a mean fraction of 26%.

[50] The overall effect from the new scheme on the sea ice albedo was largest in summer, with average reductions of 23%, or 0.14, in NH in August. In SH the overall effect was less. The melt ponds in the SH had a much shorter duration and covered less area compared to the NH, still, relatively large albedo reductions were found in the Weddell Sea, and overall the sea ice albedo in February in SH was reduced by 12%. The effect of reduced sea ice albedo was overall reduced sea ice thickness, concentration, and volume, with large temporal and spatial variations. For example, in the Barents and Okhotsk the sea ice albedo increased in March, giving an increased sea ice thickness and concentration for these areas (Figures 9, 10, and 12). In September, the pattern was spatially homogeneously with reduced albedo, thickness and concentrations for all areas where the new ALB scheme produced a significant effect.

[51] There are, however, two problems with assessing the simulations of sea ice parameters in the model and forcing used here against observational data sets. First, the observations are for present-day climate, whereas the model simulations use preindustrial climate forcings. For example, simulations suggest that mean ice thickness has declined 0.4 m since 1860 [*McLaren et al.*, 2006]. Second, the time period for the observations were relatively short, thus it may not reflect the long term state of the 50-year average we investigate.

[52] Regardless, this work is one step toward explaining and modeling the rapid melting of the Arctic sea ice. As there is a tendency that the rough MYI is being replaces by the smoother FYI, our simulations show that melt ponds may be even more important for the melting Arctic in the years to come. Hence, the inclusion of melt ponds in the description of the energy balance can be crucial for the accuracy of the GCMs in the future.

[53] **Acknowledgments.** We would like to thank Renate Brokopf for preparing the model data and Figures 8–10 and 12 and S. Gerland and M. Køltzow for comments on the work. A. C. Roesch, B. Ivanov, and D. K. Hall are acknowledged for comments during an early stage of this work. We would also like to thank the anonymous reviewers for substantially improving the paper. This work was supported by the Research Council of Norway, the Norwegian Polar Institute, and the University of Tromsø.

References

Andreas, E. L., and S. F. Ackley (1982), On the differences in ablation seasons of Arctic and Antarctic sea ice, *J. Atmos. Sci.*, *39*, 440–447.

Barber, D. G., and J. Yackel (1999), The physical, radiative and microwave scattering characteristics of melt ponds on Arctic landfast sea ice, *International Journal of Remote Sensing*, *20*(10), 2069–2090.

Barry, R. G. (1996), The parameterization of surface albedo for sea ice and its snow cover, *Prog. Phys. Geogr.*, *20*(1), 63–79.

Brandt, R. E., S. G. Warren, A. P. Worby, and T. C. Grenfell (2005), Surface albedo of the Antarctic sea ice zone, *J. Clim.*, *18*, 3606–3622.

Cavalieri, D. J., and C. L. Parkinson (2008), Antarctic sea ice variability and trends, 1979–2006, *J. Geophys. Res.*, *113*, C07004, doi:10.1029/2007JC004564.

Comiso, J. C. (2006), Abrupt decline in the Arctic winter sea ice cover, *Geophys. Res. Lett.*, *33*, L18504, doi:10.1029/2006GL027341.

Curry, J., J. L. Schramm, and E. E. Ebert (1995), Sea ice-albedo climate feedback mechanism, *J. Clim.*, *8*, 240–247.

Curry, J. A., J. L. Schramm, D. K. Perovich, and J. O. Pinto (2001), Applications of SHEBA/FIRE data to evaluation of snow/ice albedo parameterizations, *J. Geophys. Res.*, *106*(D14), 15,345–15,355.

Derksen, C., J. Piwowar, and E. LeDrew (1997), Sea-ice melt-pond fraction as determined from low level aerial photographs, *Arct. Alp. Res.*, *29*(3), 345–351.

Dickinson, R. E., A. Henderson-Sellers, P. J. Kennedy, and M. F. Wilson (1986), Biosphere Atmosphere Transfer Scheme (BATS) for the NCAR

Community Climate Model, *NCAR Tech. Note, NCAR/TN-275+STR*, 69 pp., Natl. Cent. for Atmos. Res., Boulder, Colo.

Dickinson, R. E., A. Henderson-Sellers, and P. J. Kennedy (1993), Biosphere Atmosphere Transfer Scheme (BATS) version 1e as coupled to the NCAR Community Climate Model, *NCAR Tech. Note, NCAR/TN-387+STR*, 72 pp., Natl. Cent. for Atmos. Res., Boulder, Colo.

Eicken, H., T. C. Grenfell, D. K. Perovich, J. A. Richter-Menge, and K. Frey (2004), Hydraulic controls of summer Arctic pack ice albedo, *J. Geophys. Res.*, *109*, C08007, doi:10.1029/2003JC001989.

Fetterer, F., and N. Untersteiner (1998a), Melt pond coverage statistics from classified satellite data, in *IGARSS '98: Sensing and Managing the Environment*, pp. 1954–1956, Inst. Electr. and Electron. Eng., Piscataway, N. J.

Fetterer, F., and N. Untersteiner (1998b), Observations of melt ponds on Arctic sea ice, *J. Geophys. Res.*, *103*(C11), 24,821–24,835.

Gerland, S., J. G. Winther, J. B. Ørbæk, G. E. Liston, N. A. Øritsland, A. Blanco, and B. Ivanov (1999), Physical and optical properties of snow covering Arctic tundra on Svalbard, *Hydrol. Processes*, *13*, 2331–2343.

Gerland, S., C. Haas, M. Nicolaus, and J. G. Winther (2004), Seasonal development of structure and optical properties of fast ice in Kongsfjorden, Svalbard, in *The Coastal Ecosystem of Kongsfjorden, Svalbard*, *Rep. Polar Res.*, *492*, edited by C. Wiencke, pp. 26–34, Alfred Wegner Inst. for Polar and Mar. Res., Bremerhaven, Germany.

Gerland, S., et al. (2007), Ice in the sea, in *Global Outlook for Ice and Snow*, chap. 5, pp. 63–96, U.N. Environ. Programme, Nairobi, Kenya.

Hanesiak, J. M., D. G. Barber, R. A. De Abreu, and J. J. Yackel (2001a), Local and regional albedo observations of Arctic first-year sea ice during melt ponding, *J. Geophys. Res.*, *106*(C1), 1005–1016.

Hanesiak, J. M., J. J. Yackel, and D. G. Barber (2001b), Effect of melt ponds on first-year sea ice ablation-Integration of RADARSAT-1 and thermodynamic modelling, *Can. J. Remote Sens.*, *27*(5), 433–442.

Hibler, W. D., III (1979), A dynamic thermodynamic sea ice model, *J. Phys. Oceanogr.*, *9*, 815–846.

Jungclaus, J. H., N. Keenlyside, M. Botzet, H. Haak, J. J. Luo, M. Latif, J. Marotzke, U. Mikolajewicz, and E. Roeckner (2006), Ocean circulation and tropical variability in the coupled model ECHAM5/MPI-OM, *J. Clim.*, *19*, 3952–3972.

Køltzow, M. (2007), The effect of a new snow and sea ice albedo scheme on regional climate model simulations, *J. Geophys. Res.*, *112*, D07110, doi:10.1029/2006JD007693.

Laine, V. (2004), Arctic sea ice regional albedo variability and trends, 1982–1998, *J. Geophys. Res.*, *109*, C06027, doi:10.1029/2003JC001818.

Laxon, S., N. Peacock, and D. Smith (2003), High interannual variability of sea ice thickness in the Arctic region, *Nature*, *425*(30), 947–950.

Lüthje, M., D. L. Feltham, P. D. Taylor, and M. G. Worster (2006), Modeling the summertime evolution of sea-ice melt ponds, *J. Geophys. Res.*, *111*, C02001, doi:10.1029/2004JC002818.

Markus, T., D. J. Cavalieri, and A. Ivanoff (2002), The potential of using Landsat 7 ETM+ for the classification of sea-ice surface conditions during summer, *Ann. Glaciol.*, *34*, 415–419.

Markus, T., D. J. Cavalieri, M. A. Tschudi, and A. Ivanoff (2003), Comparison of aerial video and Landsat 7 data over ponded sea ice, *Remote Sens. Environ.*, *86*(4), 458–469.

Marsland, S. J., H. Haak, J. H. Jungclaus, M. Latif, and F. Röske (2003), The Max-Planck-Institute global ocean/sea ice model with orthogonal curvilinear coordinates, *Ocean Modell.*, *5*, 91–127.

McLaren, A. J., et al. (2006), Evaluation of the sea ice simulation in a new coupled atmosphere-ocean climate model (HadGEM1), *J. Geophys. Res.*, *111*, C12014, doi:10.1029/2005JC003033.

Morassutti, M. P. (1991), Climate model sensitivity to sea ice albedo parameterization, *Theor. Appl. Climatol.*, *44*, 25–36.

Morassutti, M. P., and E. F. LeDrew (1996), Albedo and depth of melt ponds on sea ice, *Int. J. Climatol.*, *16*, 817–838.

Overland, J. E., and M. Wang (2007), Future regional Arctic sea ice declines, *Geophys. Res. Lett.*, *34*, L17705, doi:10.1029/2007GL030808.

Pedersen, C. A., and J.-G. Winther (2005), Intercomparison and validation of snow albedo parameterisation schemes in climate models, *Clim. Dyn.*, *25*, 351–362.

Pedersen, C. A., F. Godtliebsen, and A. C. Roesch (2008), A scale-space approach for detecting significant differences between models and observations using global albedo distributions, *J. Geophys. Res.*, *113*, D10108, doi:10.1029/2007JD009340.

Pedersen, C. A., R. Hall, S. Gerland, A. H. Sivertsen, T. Svenøe, and C. Haas (2009), Combined airborne profiling over Fram Strait sea ice: Fractional sea-ice types, albedo and thickness measurements, *Cold Reg. Sci. Technol.*, *55*, 23–32.

Perovich, D. K., and W. B. Tucker III (1997), Arctic sea-ice conditions and the distribution of solar radiation during summer, *Ann. Glaciol.*, *25*, 445–450.

Perovich, D. K., et al. (1999), Year on ice gives climate insights, *Eos Trans. AGU*, *80*(41), 481.

Perovich, D. K., T. C. Grenfell, B. Light, and P. V. Hobbs (2002a), Seasonal evolution of the albedo of multiyear Arctic sea ice, *J. Geophys. Res.*, *107*(C10), 8044, doi:10.1029/2000JC000438.

Perovich, D. K., W. B. Tucker III, and K. A. Ligett (2002b), Aerial observations of the evolution of ice surface conditions during summer, *J. Geophys. Res.*, *107*(C10), 8048, doi:10.1029/2000JC000449.

Podgorny, I. A., and T. C. Grenfell (1996), Partitioning of solar energy in melt ponds from measurements of pond albedo and depth, *J. Geophys. Res.*, *101*(C10), 22,737–22,748.

Rayner, N. A., D. E. Parker, E. B. Horton, C. K. Folland, L. V. Alexander, D. P. Rowell, E. C. Kent, and A. Kaplan (2003), Global analyses of sea surface temperature, sea ice, and night marine air temperature since the late nineteenth century, *J. Geophys. Res.*, *108*(D14), 4407, doi:10.1029/2002JD002670.

Roeckner, E., et al. (2003), The atmospheric general circulation model ECHAM5-Part 1, *Tech. Rep. 349*, Max Planck Inst. for Meteorol., Hamburg.

Roeckner, E., R. Brokopf, M. Esch, M. Giorgetta, S. Hagemann, L. Kornblueh, E. Manzini, U. Schlese, and U. Schulzweida (2006), Sensitivity of simulated climate to horizontal and vertical resolution in the ECHAM5 atmosphere model, *J. Clim.*, *19*, 3771–3791.

Roesch, A. C. (2000), Assessment of the land surface scheme in climate models with focus on surface albedo and snow cover, Ph.D. thesis, ETH Zurich, Zurich, Switzerland.

Roesch, A., M. Wild, H. Gilgen, and A. Ohmura (2001), A new snow cover fraction parameterisation for the ECHAM4 GCM, *Clim. Dyn.*, *17*, 933–946.

Schramm, J. L., M. M. Holland, J. A. Curry, and E. E. Ebert (1997), Modeling the thermodynamics of a sea-ice thickness distribution: 1. Sensitivity to ice thickness resolution, *J. Geophys. Res.*, *102*(C10), 23,079–23,091.

Solomon, S., et al. (2007), Technical summary, in *Climate Change 2007: The Physical Science Basis-Contribution of Working Group I to the Fourth Assessment Report of the Intergovernmental Panel on Climate Change*, pp. 19–91, Cambridge Univ. Press, Cambridge, U. K.

Stroeve, J., M. M. Holland, W. Meier, T. Scambos, and M. Serreze (2007), Arctic sea ice decline: Faster than forecast, *Geophys. Res. Lett.*, *34*, L09501, doi:10.1029/2007GL029703.

Taylor, P. D., and D. L. Feltham (2004), A model of melt pond evolution on sea ice, *J. Geophys. Res.*, *109*, C12007, doi:10.1029/2004JC002361.

Tschudi, M. A., J. A. Curry, and J. A. Maslanik (1997), Determination of areal surface-feature coverage in the Beaufort Sea using aircraft video data, *Ann. Glaciol.*, *25*, 434–438.

Tschudi, M. A., J. A. Curry, and J. A. Maslanik (2001), Airborne observations of summertime surface features and their effect on surface albedo during FIRE/SHEBA, *J. Geophys. Res.*, *106*(D14), 15,335–15,344.

Tucker, W. B., III, A. J. Gow, D. A. Meese, and H. W. Bosworth (1999), Physical characteristics of summer sea ice across the Arctic Ocean, *J. Geophys. Res.*, *104*, 1489–1504.

Wang, S., A. P. Trishchenko, K. V. Khlopenkov, and A. Davidson (2006), Comparison of International Panel on Climate Change Fourth Assessment Report climate model simulations of surface albedo with satellite products over northern latitudes, *J. Geophys. Res.*, *111*, D21108, doi:10.1029/2005JD006728.

Wiscombe, W. J., and S. G. Warren (1980), A model for the spectral albedo of snow. I: Pure snow, *J. Atmos. Sci.*, *37*, 2712–2733.

Yackel, J. J., and D. G. Barber (2000), Melt ponds on sea-ice in the Canadian Archipelago: 2. On the use of RADARSAT-1 synthetic aperture radar for geophysical inversion, *J. Geophys. Res.*, *105*(C9), 22,061–22,070.

Yackel, J. J., D. G. Barber, and J. M. Hanesiak (2000), Melt ponds on sea-ice in the Canadian Archipelago: 1. Variability in morphological and radiative properties, *J. Geophys. Res.*, *105*(C9), 22,049–22,060.

Yang, Z. L., R. E. Dickinson, A. Robock, and K. Y. Vinnikov (1997), Validation of the snow submodel of the biosphere-atmosphere transfer scheme with Russian snow cover and meteorological observational data, *J. Clim.*, *10*, 353–373.

M. Lüthje, SINTEF Petroleum Research, Prof. Olav Hanssens vei 7A, N-4068, Stavanger, Norway. (mikael@lythje.com)

C. A. Pedersen and J.-G. Winther, Norwegian Polar Institute, N-9296 Tromsø, Norway. (christina@npolar.no; winther@npolar.no)

E. Roeckner, Max Planck Institute for Meteorology, D-20146 Hamburg, Germany. (erich.roeckner@zmaw.de)